Supporting Information (JA-2008-00109u)

Alpha-CuV_2O_6 Nanowires: Hydrothermal Synthesis and Primary Lithium-Battery Application

*Hua Ma, Shaoyan Zhang, Weiqiang Ji, Zhanliang Tao, and Jun Chen**

Key Laboratory of Energy-Material Chemistry (Tianjin) and Engineering Research Center of Energy Storage & Conversion (Ministry of Education), Chemistry College, Nankai University, Tianjin 300071, People's Republic of China

*E-mail: chenabc@nankai.edu.cn

CONTENTS:

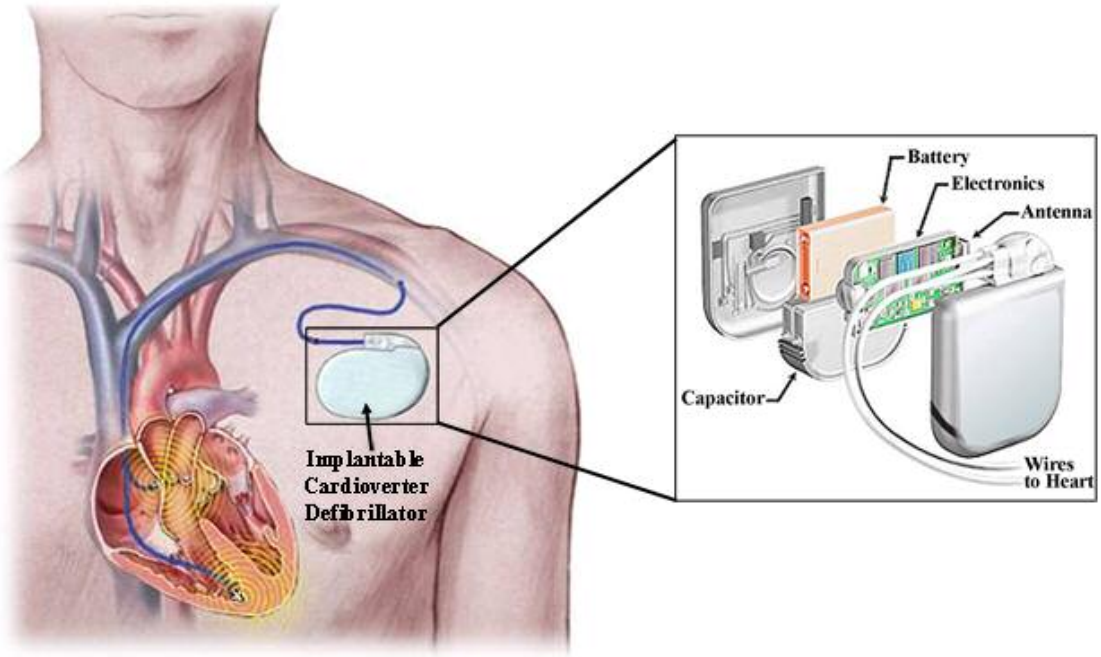

Figure S1. The illustration of working principle of the implantable cardioverter defibrillator (ICD) (left picture) and its configuration (right picture). An ICD consists of a battery and electrical circuitry (pulse generator) connected to one or more insulated wires. The pulse generator and batteries are sealed together and implanted under the skin, usually near the shoulder. The wires are threaded through blood vessels from the ICD to the heart muscle. The ICD continuously checks the heart rate. When it detects a too-rapid or irregular heartbeat, it delivers a shock that resets the heart to a more normal rate and electrical pattern. The battery is capable of supplying a continuous low-current drain on the order of microamperes to power monitoring circuits and rapidly providing high-current pulses at ampere level on demand to charge capacitors quickly.

(see website, http://www.fda.gov/hearthealth/treatments/medicaldevices/icd.html, and http://www.guidantlawyers.com/defibrillator_functions.html).

Figure S2. The photograph of the experimental setup, including a teflon vessel and a stainless steel autoclave.

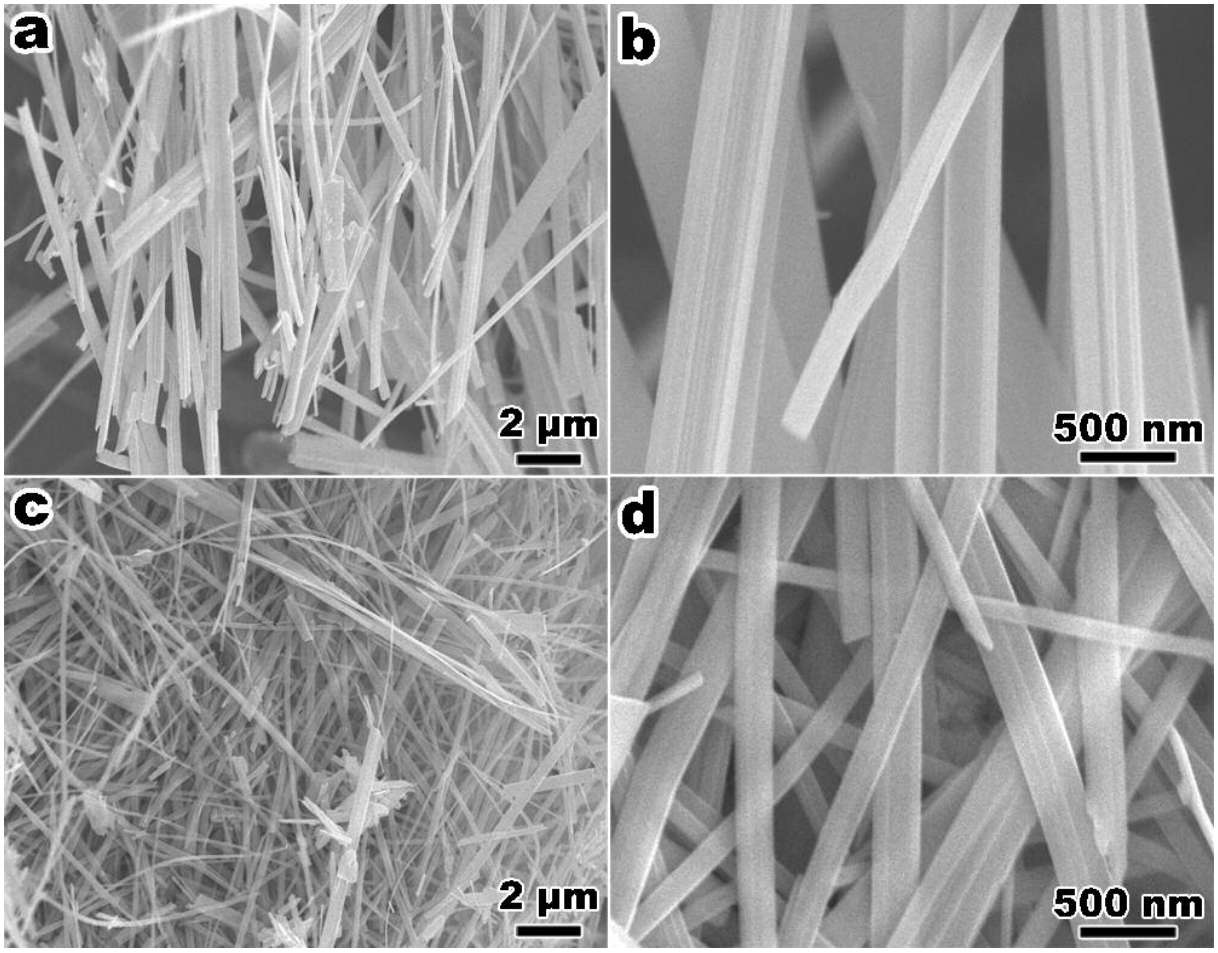

Figure S3. SEM images of the α-CuV_2O_6 samples synthesized from (a, b) 0.03 and (c, d) 0.1 mol/L $CuCl_2$ solution at 210 ºC for 12 h.

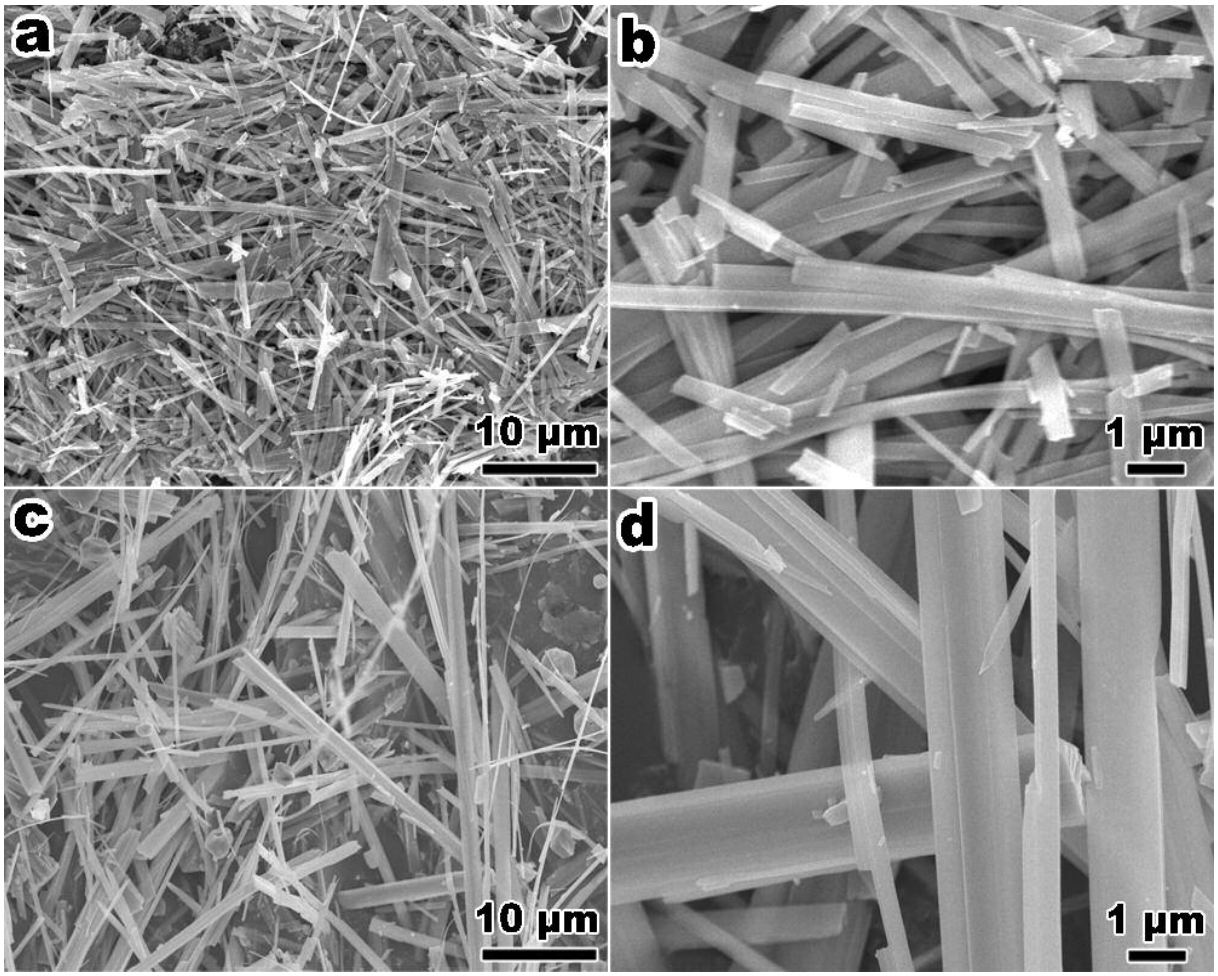

Figure S4. SEM images of the α-CuV_2O_6 samples synthesized from (a, b) 0.15 and (c, d) 0.01 mol/L $CuCl_2$ solution at 210 ºC for 12 h.

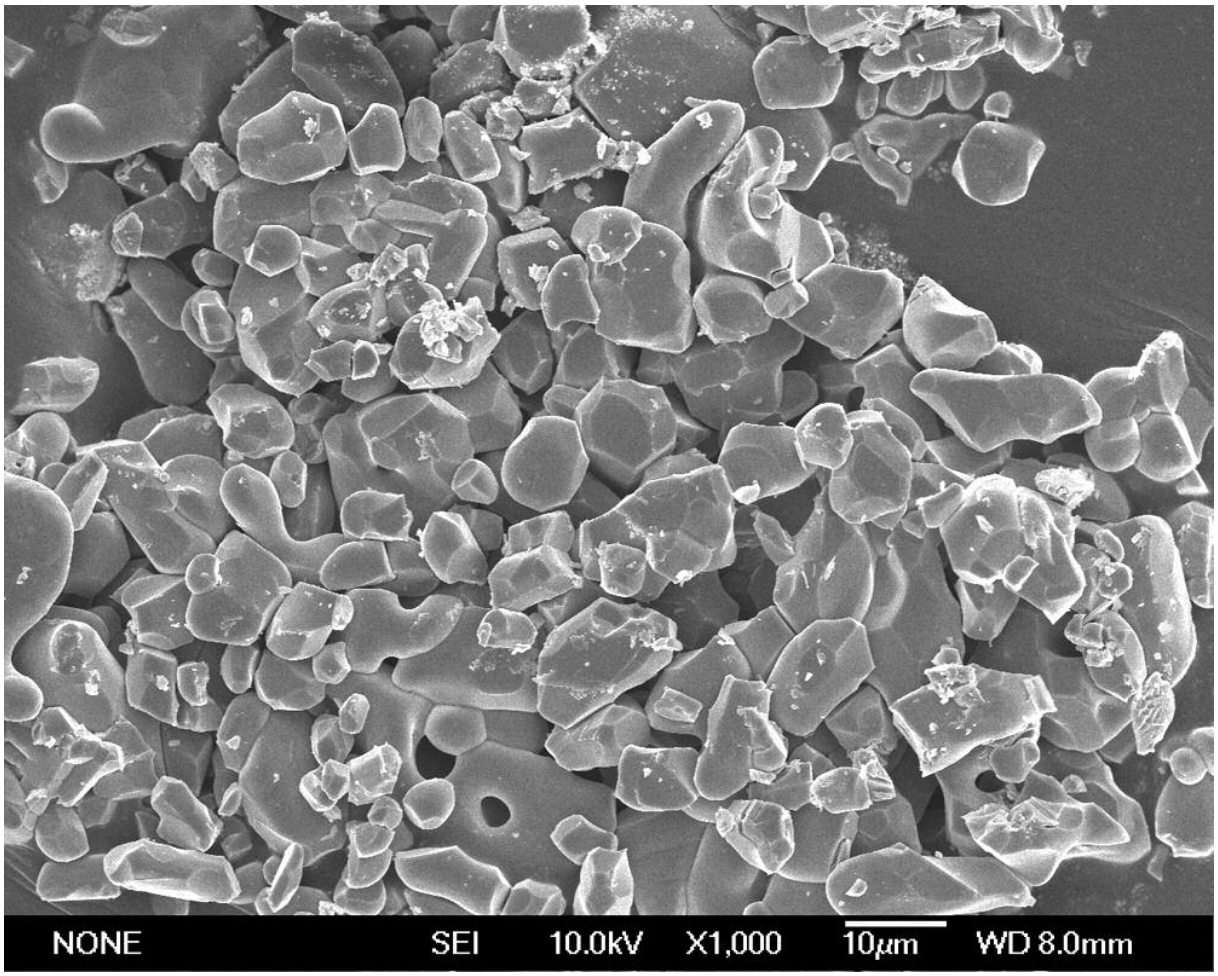

Figure S5. SEM images of α-CuV_2O_6 bulk particles obtained from solid-state reaction.

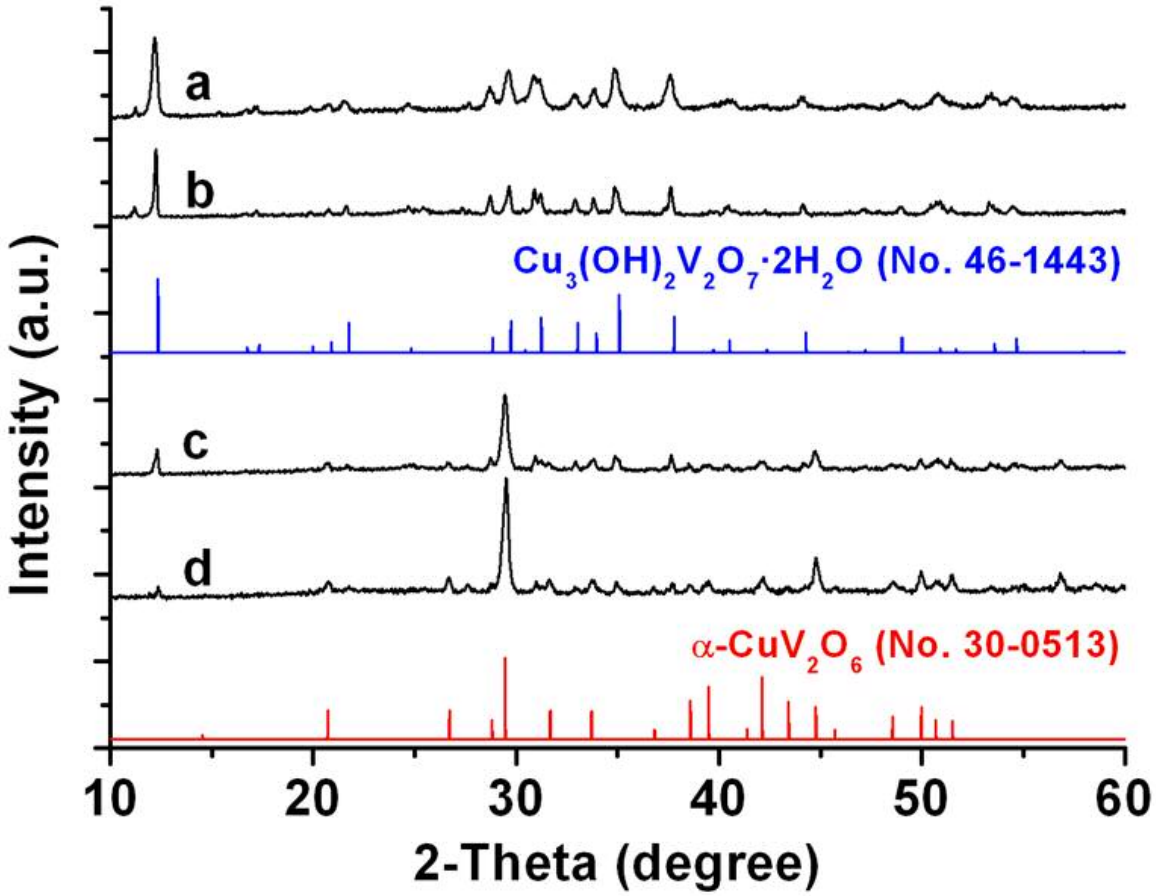

Figure S6. The XRD patterns of the as-synthesized samples obtained (a) before and after hydrothermal treatment at 210 ºC for (b) 1 h, (c) 3 h and (d) 6 h.

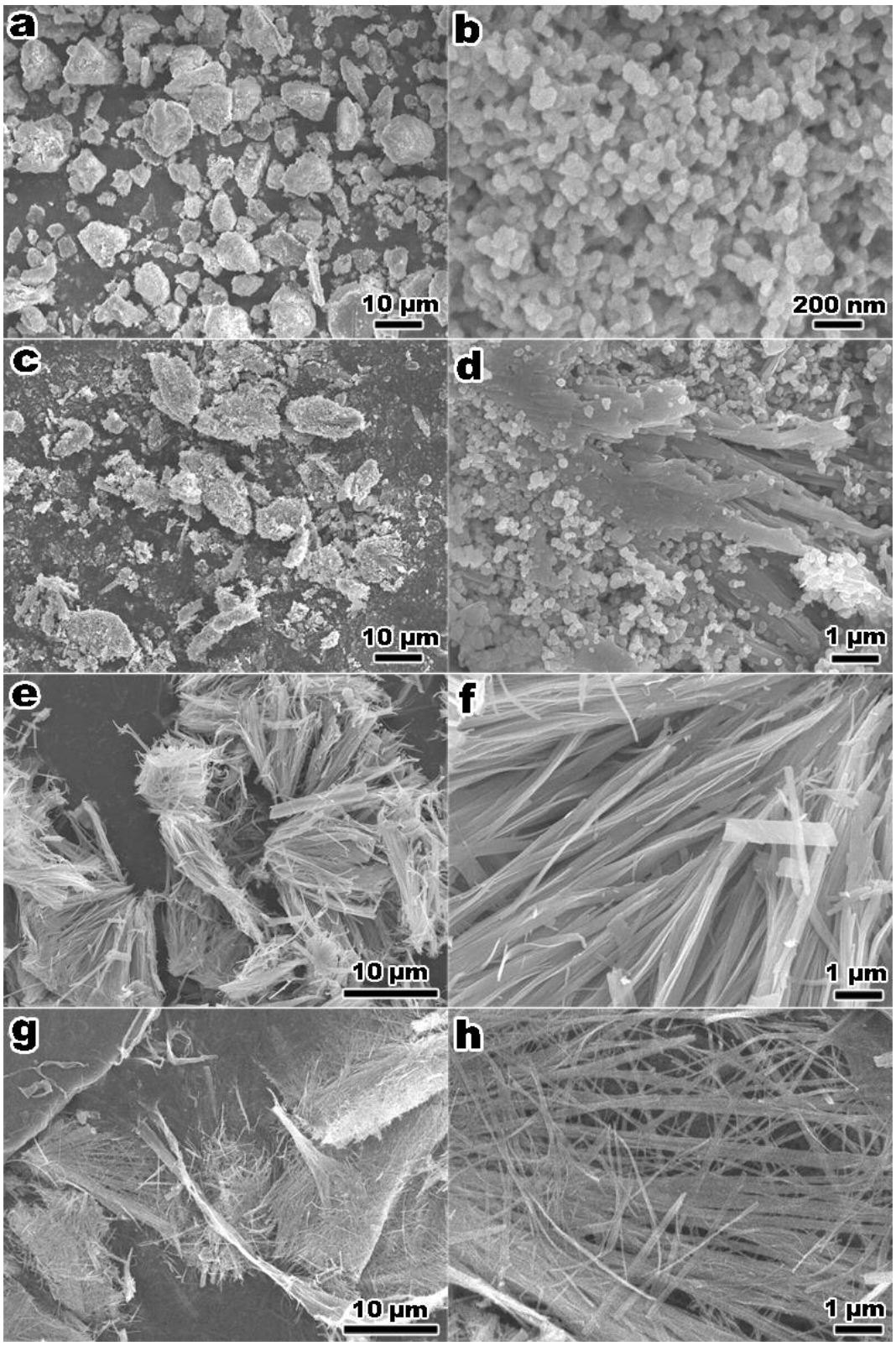

Figure S7. The SEM images of the as-synthesized α-CuV_2O_6 samples obtained (a, b) before and after hydrothermal treatment at 210 ºC for (c, d) 1 h, (e, f) 3 h and (g, h) 6 h.

Figure S6 shows the XRD patterns and Figure S7 shows the SEM images of the products obtained at 210 ºC for differernt reaction time. Initially, the direct mixing of $CuCl_2$ and NH_4VO_3 solution immediately led to the formation of an orange precipitate. All the diffraction peaks of the initial precipitate (Figure S6a) can be indexed to a pure crystalline phase of $Cu_3(OH)_2V_2O_7{\cdot}2H_2O$ (JCPDS Card No. 46-1443). This sample was composed of nanoparticles with the dimater of about 50 nm (Figure S7a-b). After hydrothermal treatment for 1h, the intensity of the diffraction peaks of $Cu_3(OH)_2V_2O_7{\cdot}2H_2O$ was decreased (Figure S5b) and the lamellar structure was formed (Figure S7c-d). When the reaction time was prolonged to 3 h, a new crystal phase, which can be ascribed to α-CuV_2O_6 (JCPDS Card No. 30-0513), began to coexist with $Cu_3(OH)_2V_2O_7{\cdot}2H_2O$, and the intensity of the diffraction peaks of $Cu_3(OH)_2V_2O_7{\cdot}2H_2O$ further increased (Figure S6c). Furthermore, Figure S7e-f confirmed that the lamellar structure began to split into nanosheets. With the reaction processing (6h), the intensity of the diffraction peaks of α-CuV_2O_6 increased; while the diffraction peaks of $Cu_3(OH)_2V_2O_7{\cdot}2H_2O$ were barely observed (Figure S6d), indicating that $Cu_3(OH)_2V_2O_7{\cdot}2H_2O$ was an intermediate phase in the reaction. Figure S7g-h demonstrates that the nanosheets can further be split themselves into nanowires. Then the proportion of the nanowires in the product increased with increasing the reaction time, and finally the product became α-CuV_2O_6 nanowires after 12 h, as shown in Figure 2.

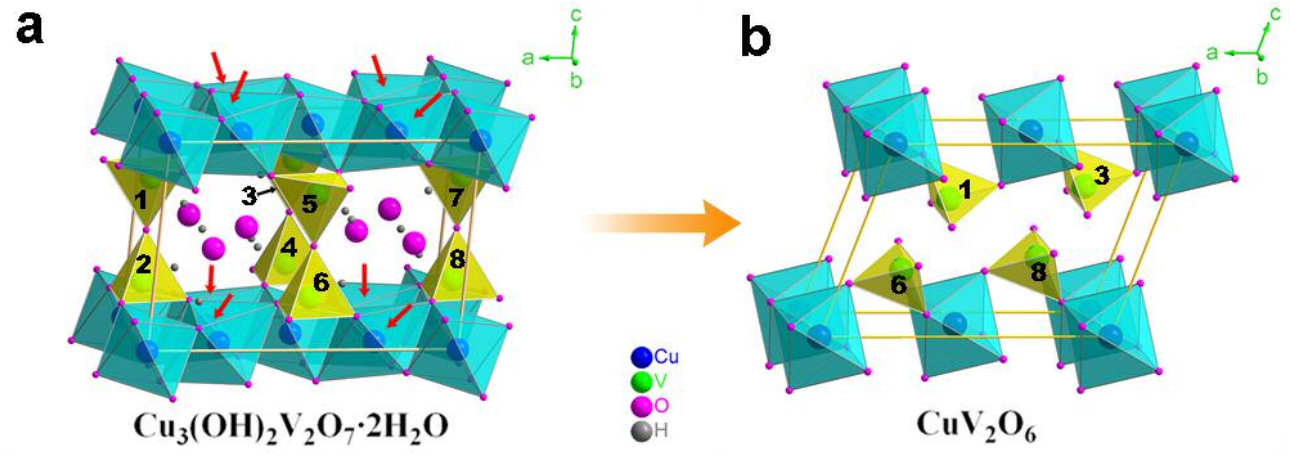

Figure S8. Schematic illustration of the possible phase transformation in the synthesis of α-CuV_2O_6 nanowires. The crystal structure of (a) $Cu_3(OH)_2V_2O_7{\cdot}2H_2O$ and (b) α-CuV_2O_6.

The phase transformation from $Cu_3(OH)_2V_2O_7{\cdot}2H_2O$ to α-CuV_2O_6 was illustrated in Figure S8. Initially, the interlayer spaces in the layered structure of $Cu_3(OH)_2V_2O_7{\cdot}2H_2O$ are occupied by H_2O molecular.[S1] With reaction going on, the H_2O molecular deintercalates gradually from the layer, leading to the contraction and distortion of the structure. At this condition, per Cu^{2+} ion with one O^{2-} in the octahedrons indicated by the red arrows removes from the copper-oxygen octahedra layer to produce CuO. Meanwhile, the vanadium-oxygen octahedral migrates to the new position (No. 1, 3, 6 and 8 are still in the original unit cell; Meanwhile, No. 2, 4, 5 and 7 move into the adjacent unit cell). Finally, the α-CuV_2O_6 was formed after the phase transformation.

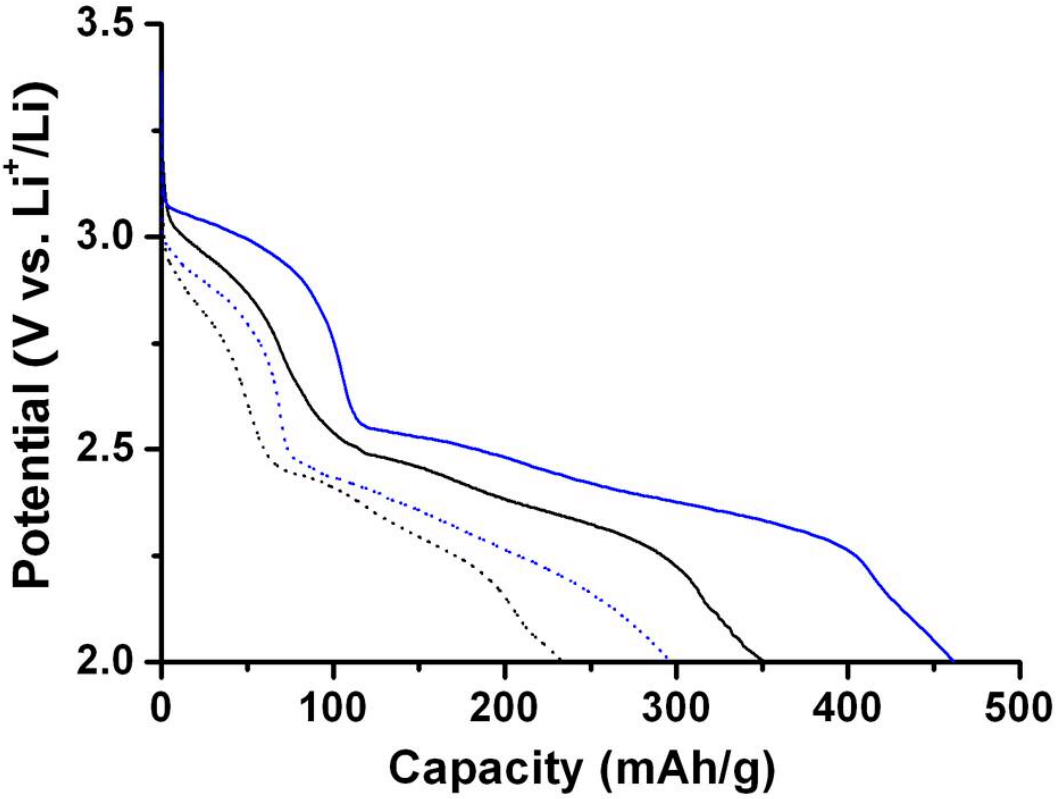

Figure S9. Discharge curves of the cells made of the as-prepared α-CuV_2O_6 nanowires (solid) and bulk particles (dot) at 37 ºC. Current densities: 40 mA/g (blue), 80 mA/g (black).

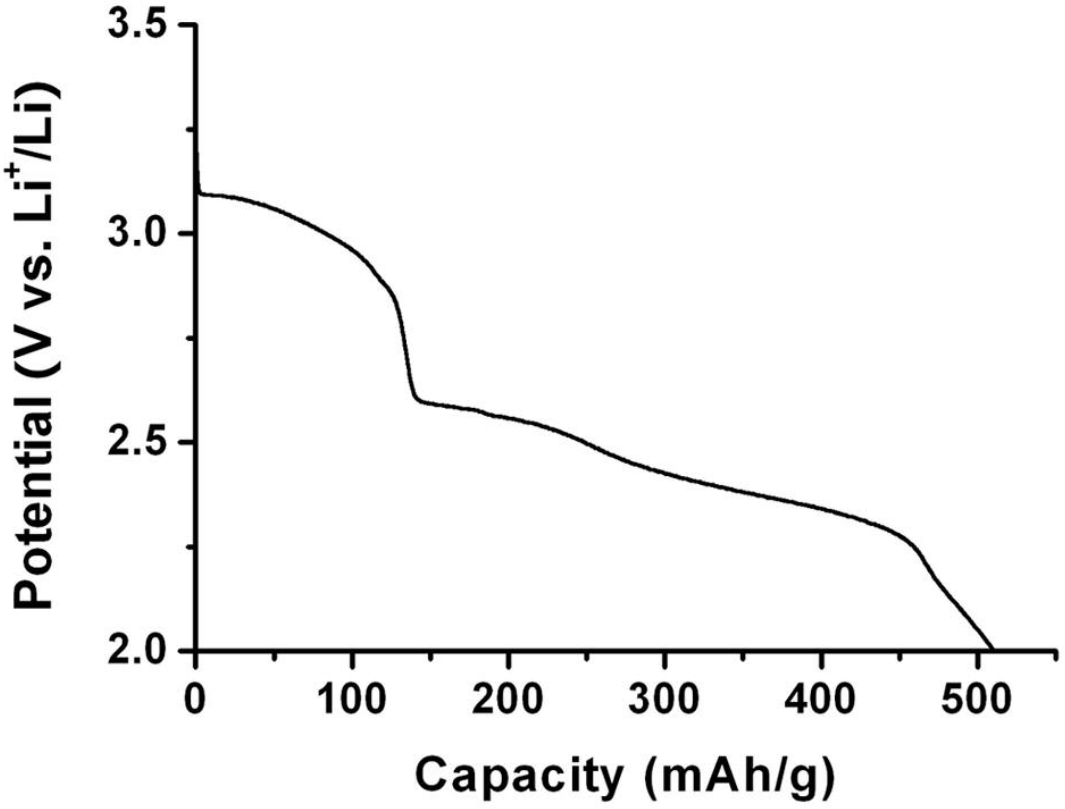

Figure S10. Discharge curve of the cell made from the as-prepared α-CuV_2O_6 nanowires at the current density of 20 mA/g after the cell equilibrated at 37 ^oC for two months. The discharge capacity is about 510 mAh/g.

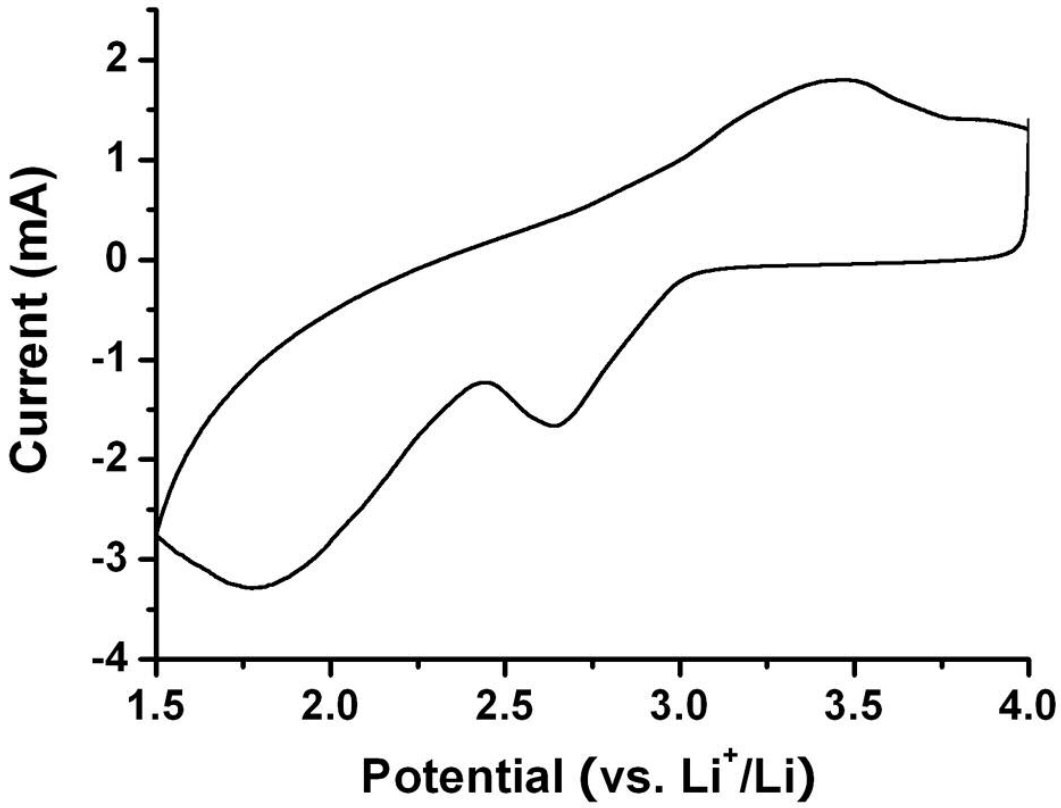

Figure S11. CV of the electrode made from α-CuV_2O_6 nanowires in the first cycle at a scan rate of 1.0 mV/s and the temperature of 37 °C with the potential range of 4.0 ~ 1.5 V vs. Li^+/Li.

In the cathodic polarization process, two peaks were observed at about 2.64 and 1.79 V vs. Li^+/Li, respectively, which can be assigned to and the reduction of Cu^{2+} and V^{5+} due to the lithium intercalation. During the following anodic polarization, one broad peak was observed at around 3.46 V, which is designated to the lithium extraction process. This CV curve reflects some reversibility of the lithium intercalation/deintercalation.

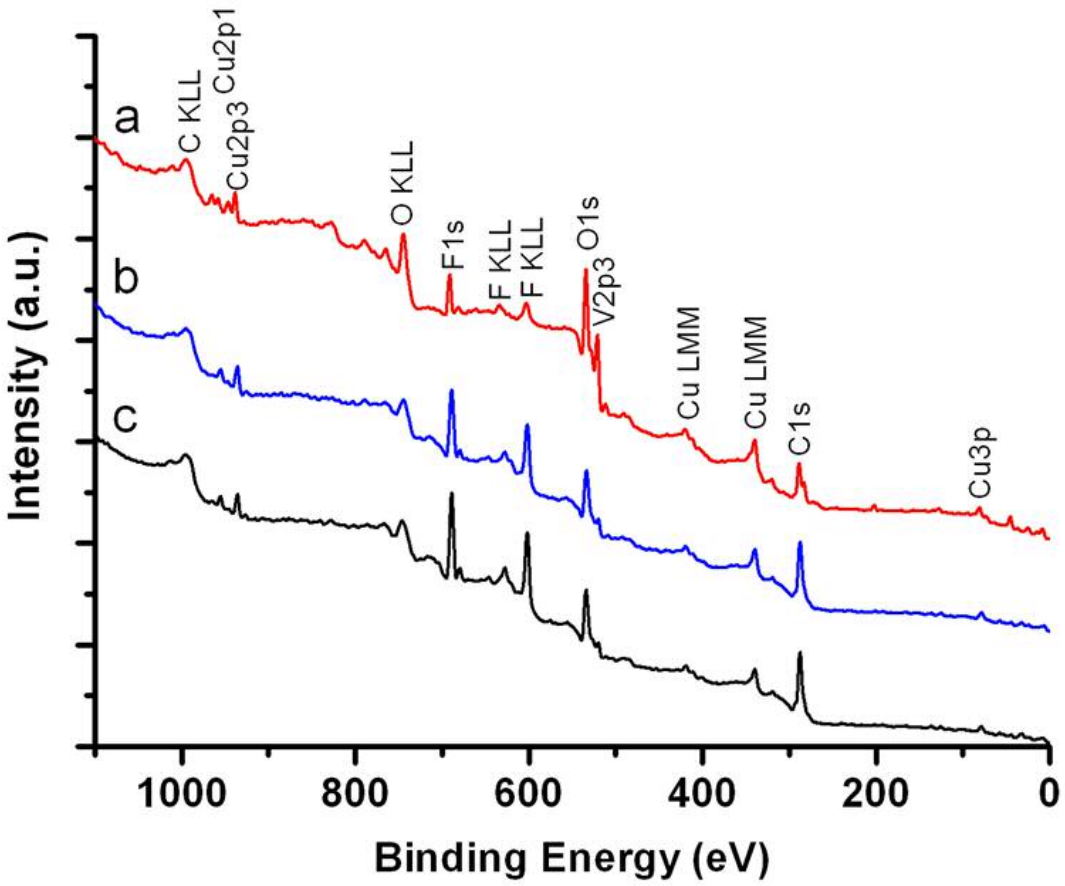

Figure S12. The survey XPS spectra of the electrode made from α-CuV_2O_6 nanowires at different discharge states: (a) before discharging, (b) 2.8 V and (c) 2.3 V. The spectra of C and F arise from the carbon black and PTFE in the electrode.

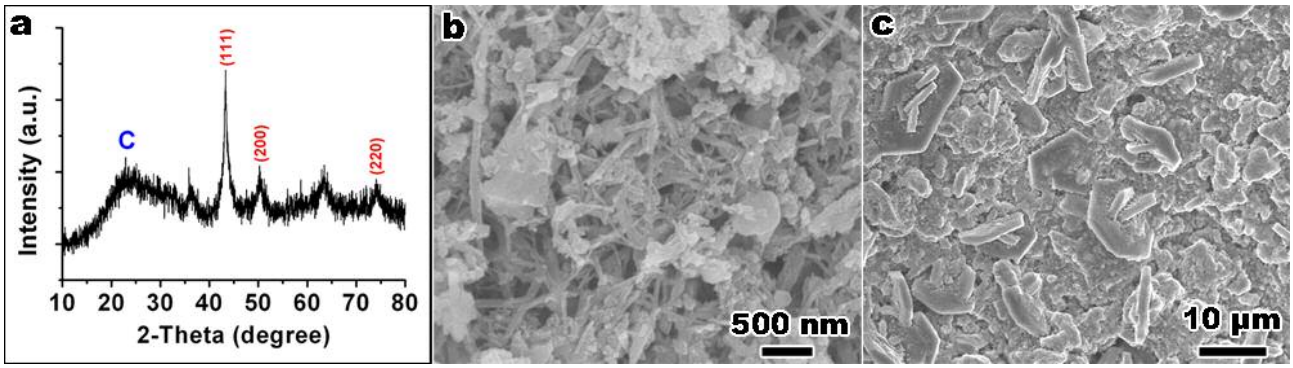

Figure S13. (a) XRD pattern, (b) SEM image of the α-CuV_2O_6 nanowires electrode and (c) SEM image of the α-CuV_2O_6 bulk particles electrode after discharging to the cut-off voltage of 2.0V.

Figure S13 shows the XRD pattern and SEM images of the electrodes of α-CuV_2O_6 nanowires and bulk particles obtained at the end of discharge. It can be seen that the peaks at 2θ=43º, 50º and 74º can be indexed to the diffraction peaks of metallic Cu (111), (200) and (220), respectively (JCPDS-ICDD Card No. 04-0836). In addition, a broad peak at about 23º arises from the amorphous carbon black used in the electrode. Furthermore, two weak peaks at 36º and 63º possibly correspond to lithiated α-CuV_2O_6. It is difficult to retrieve the crystal structure due to the broad and weak diffrcation peaks. The SEM images showed that α-CuV_2O_6 nanowires still retained their primary 1-D morphology (Figure S13b), whereas, the α-CuV_2O_6 bulk particles were decomposed to sheet-like structures at the end of discharge (Figure S13c).

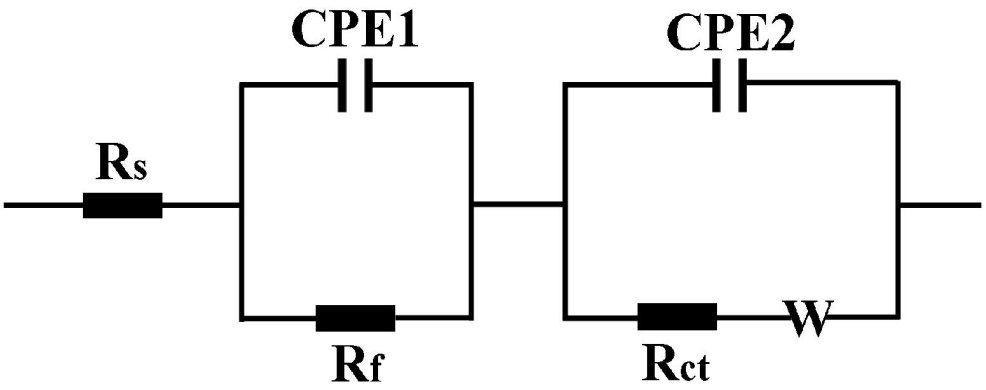

Figure S14. The equivalent circuit for the electrochemical impedance spectrum. It consists of the electrolyte (R_s), surface film (R_f) and charge transfer (R_{ct}) resistances, constant phase elements (CPE_1 and CPE_2), along with the Warburg impedance (W).

Table S1. Charge-transfer resistance (R_{ct}) and exchange current (i_0) of the electrodes with α-CuV_2O_6 nanowires and bulk particles measured at different discharge states and temperatures.

Sample	Voltage	R_{ct} (Ohm)				i_0 (mA)			
	(V)	25 ºC	37 ºC	45 ºC	55 ºC	25 ºC	37 ºC	45 ºC	55 ºC
Nanowires	2.8	162.1	83.8	64.8	40.8	0.158	0.319	0.423	0.693
	2.3	97	57.1	42.7	28.3	0.265	0.468	0.642	0.999
Bulk particles	2.8	281.7	129.3	92.8	50.01	0.091	0.207	0.295	0.565
	2.3	201.5	108	76.7	41.6	0.127	0.247	0.357	0.679

Supporting Reference

(S1) Lafontaine, M. A.; Le Bail, A.; Férey, G. *J. Solid State Chem*. **1990**, *85*, 220-227.